Article

Spectroscopic and Electronic Structure Studies of 2,3-Dihydroxybiphenyl 1,2-Dioxygenase: O Reactivity of the Non-Heme Ferrous Site in Extradiol Dioxygenases

Mindy I. Davis, Erik C. Wasinger, Andrea Decker, Monita Y. M. Pau, Frdric H. Vaillancourt, Jeffrey T. Bolin, Lindsay D. Eltis, Britt Hedman, Keith O. Hodgson, and Edward I. Solomon

J. Am. Chem. Soc., **2003**, 125 (37), 11214-11227• DOI: 10.1021/ja029746i • Publication Date (Web): 19 August 2003

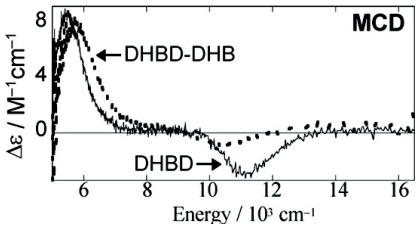

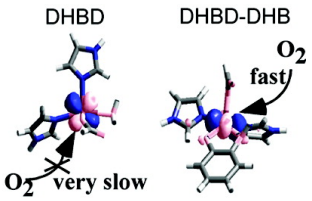

More About This Article

Additional resources and features associated with this article are available within the HTML version:

- Supporting Information
- Links to the 5 articles that cite this article, as of the time of this article download
- Access to high resolution figures
- Links to articles and content related to this article
- Copyright permission to reproduce figures and/or text from this article

View the Full Text HTML

J|A|C|S
ARTICLES
Published on Web 08/19/2003

Spectroscopic and Electronic Structure Studies of 2,3-Dihydroxybiphenyl 1,2-Dioxygenase: O_2 Reactivity of the Non-Heme Ferrous Site in Extradiol Dioxygenases

Mindy I. Davis,[†] Erik C. Wasinger,[†] Andrea Decker,[†] Monita Y. M. Pau,[†] Frédéric H. Vaillancourt,[§] Jeffrey T. Bolin,*[,⊥] Lindsay D. Eltis,*[,§,||] Britt Hedman,*[,†,‡] Keith O. Hodgson,*[,†,‡] and Edward I. Solomon*[,†]

Contribution from the Department of Chemistry and Stanford Synchrotron Radiation Laboratory, Stanford University, Stanford, California 94305-5080, Departments of Microbiology and Biochemistry, University of British Columbia, Vancouver, Canada, V6T 1Z3, Department of Biochemistry, Pavillon Marchand, Université Laval, Quebec City, Quebec, G1K 7P4, Canada, and Markey Center for Stuctural Biology, Department of Biological Sciences, Purdue University, West Lafayette, Indiana 47907-1392

Received December 13, 2002; E-mail: edward.solomon@stanford.edu

Abstract: The extradiol dioxygenase, 2,3-dihydroxybiphenyl 1,2-dioxygenase (DHBD, EC 1.13.11.39), has been studied using magnetic circular dichroism (MCD), variable-temperature variable-field (VTVH) MCD, X-ray absorption (XAS) pre-edge, and extended X-ray absorption fine structure (EXAFS) spectroscopies, which are analogous to methods used in earlier studies on the extradiol dioxygenase catechol 2,3-dioxygenase [Mabrouk et al. *J. Am. Chem Soc.* **1991**, *113*, 4053−4061]. For DHBD, the spectroscopic data can be correlated to the results of crystallography and with the results from density functional calculations to obtain detailed geometric and electronic structure descriptions of the resting and substrate (DHB) bound forms of the enzyme. The geometry of the active site of the resting enzyme, square pyramidal with a strong Fe−glutamate bond in the equatorial plane, localizes the redox active orbital in an orientation appropriate for O_2 binding. However, the O_2 reaction is not favorable, as it would produce a ferric superoxide intermediate with a weak Fe−O bond. Substrate binding leads to a new square pyramidal structure with the strong Fe−glutamate bond in the axial direction as indicated by a decrease in the ^5E_g and increase in the $^5T_{2g}$ splitting. Electronic structure calculations provide insight into the relative lack of dioxygen reactivity for the resting enzyme and its activation upon substrate binding.

Introduction

Catechols are common intermediary catabolites in the aerobic microbial degradation of aromatic compounds.[1−3] The enzymes that degrade these catabolites, the catechol dioxygenases, can be divided into two broad classes based on the position of ring cleavage: intradiol and extradiol dioxygenases. The intradiol dioxygenases utilize a high-spin ferric center to cleave the catechol ring between the two adjacent hydroxylated carbons with insertion of both atoms from dioxygen. In contrast, extradiol dioxygenases utilize a high-spin ferrous center to cleave the catechol substrate specifically on either the distal or the proximal side of the hydroxyl groups. These differences in iron oxidation state and ring cleavage position are manifestations of the different mechanisms utilized by these two classes of enzymes. Thus, in intradiol dioxygenases, substrate binding to the ferric center leads to activation of the substrate for direct attack by dioxygen, while in the extradiol dioxygenases, substrate binding to the iron activates the ferrous center for dioxygen binding.[3−6]

Extradiol dioxygenases have been historically less well characterized than intradiol dioxygenases due to the lack of any pronounced spectral features in the visible absorption region. However, in recent years, significant progress has been made in the understanding of extradiol dioxygenases. Type I and type II extradiol dioxygenases utilize the same mechanism but have different protein tertiary structures.[7] 2,3-Dihydroxybiphenyl 1,2-dioxygenase (DHBD, EC 1.13.11.39), the focus of this paper, is involved in the aerobic degradation of biphenyl (2,3-dihydroxybiphenyl, DHB, to 2-hydroxy-6-oxo-6-phenylhexa-

[†] Stanford University.
[‡] Stanford Synchrotron Radiation Laboratory.
[§] University of British Columbia.
[||] Université Laval.
[⊥] Purdue University.

(1) Dagley, S. In *The Bacteria*; Sokatch, J. R., Ornston, L. N., Eds.; Academic Press: Orlando, 1986; Vol. 10, Chapter 10, pp 527−555.
(2) Levin, M. A.; Gealt, M. A. In *Biotreatment of Industrial and Hazardous Waste*; Levin, M. A., Gealt, M. A., Eds.; McGraw-Hill: New York, 1993; pp 5−7.
(3) Lipscomb, J. D.; Orville, A. M. In *Degradation of Environmental Pollutants by Microorganisms and Their Metalloenzymes*; Sigel, H., Sigel, A., Eds.; Marcel Dekker: New York, 1992; Vol. 28, pp 243−298.
(4) Que, L., Jr.; Ho, R. Y. N. *Chem. Rev.* **1996**, *96*, 2607−2624.
(5) Solomon, E. I.; Brunold, T.; Davis, M. I.; Kemsley, J. N.; Lee, S.-K.; Lehnert, N.; Neese, F.; Skulan, A. J.; Yang, Y.-S.; Zhou, J. *Chem. Rev.* **2000**, *100*, 235−349.
(6) Bugg, T. D. H.; Winfield, C. J. *Nat. Prod. Rep.* **1998**, *5*, 513−530.
(7) Eltis, L. D.; Bolin, J. T. *J. Bacteriol.* **1996**, *178*, 5930−5937.

10.1021/ja029746i CCC: $25.00

Scheme 1. Substrate Binding to DHBD (Reproduced with permission from Solomon, E. I.; Brunold, T.; Davis, M. I.; Kemsley, J. N.; Lee, S.-K.; Lehnert, N.; Neese, F.; Skulan, A. J.; Yang, Y.-S.; Zhou, J. Chem. Rev. **2000**, *100*, 235−349. Copyright 2000 American Chemical Society)

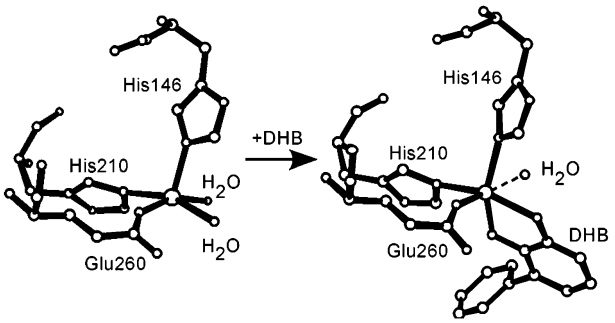

2,3-dienoate) as well as transformation of the pollutants, polychlorinated biphenyls or PCBs.[8] MCD spectroscopy has previously been applied to the extradiol dioxygenase catechol 2,3-dioxygenase (2,3-CTD) and showed prior to crystallographic results that the resting site is five-coordinate square pyramidal and that the site adopts a different five-coordinate square pyramidal structure upon substrate binding.[9] X-ray crystallographic structures are now available for two type I enzymes, DHBD (*Burkholderia sp.* LB400 and *Pseudomona*s sp. KKS102)[10−12] and catechol 2,3-dioxygenase (2,3-CTD, EC 1.13.11.2, *Pseudomonas putida* mt-2),[13] and one type II enzyme, protocatechuate 4,5-dioxygenase (4,5-PCD, EC 1.13.11.8, *Sphingomonas paucimobil*is SYK-6).[14] The crystallographically characterized ferrous active site of DHBD (LB400, 1.9 Å resolution) shows a five-coordinate square pyramidal structure with an axial histidine, an equatorial histidine, a monodentate glutamate, and two waters as equatorial ligands (Scheme 1).[10,12]

The aerobically oxidized ferric DHBD has the same coordination geometry as the reduced site but with slightly altered bond lengths.[11] It is interesting to note that, in contrast to the intradiol dioxygenases,[15] the change in oxidation state does not alter the coordination number of the site. The coordination by two histidines and a glutamate makes this enzyme part of the group of ferrous enzymes that share a common 2-His, 1-carboxylate facial triad geometry.[16] Other such enzymes include the ring-hydroxylating Rieske dioxygenases, pterin-dependent hydroxylases, β-lactam antibiotic synthases, α-ketoglutarate-dependent dioxygenases, and ethylene forming enzyme.[17] The substrate DHB has been shown by X-ray crystallography to bind asymmetrically to the iron center of DHBD in a bidentate fashion (Fe−O(cat): 2.0 and 2.4 Å), displacing one of the waters completely and with the remaining water (trans to the glutamate) at a long bond length of 2.42 Å (Scheme 1). In both structures, the site is best described as square pyramidal consistent with the MCD results on 2,3-CTD-catechol.[9,18] The substrate was shown by electronic absorption and UV resonance Raman (rR) spectroscopies to be bound as a monoanion,[18] leading to a net neutrally charged site. The crystal structure of ferric DHBD-DHB is also five-coordinate, but the structure was described as trigonal bipyramidal.[11] Magnetic Mössbauer spectroscopy of 4,5-PCD revealed that the site remains high-spin ferrous upon substrate binding with no large changes in the active-site parameters.[19] The EXAFS data show a split in the first shell in 2,3-CTD-catechol,[20,21] which is likely due to the asymmetric binding of the substrate.

In contrast to the intradiol dioxygenases,[22] intermediates have not yet been observed for the extradiol dioxygenases. The kinetics of dioxygen binding to both resting and substrate-bound extradiol dioxygenases indicate a dramatic increase in affinity upon substrate binding and implicate a ternary enzyme−substrate−O_2 complex.[23,31] Some of the enzymes such as 2,3-CTD (*P. putida* mt-2) are relatively stable in the five-coordinate resting ferrous form for extended periods of time.[24] The affinity for the dioxygen mimic NO also increases over 100- to 1000-fold upon binding catechol.[25] The origin of this relative lack of small molecule reactivity and dramatic increase upon substrate binding is one important goal of this work.

In this study of DHBD and DHBD-DHB, circular dichroism (CD), magnetic CD (MCD), variable-temperature, variable-field (VTVH) MCD, X-ray absorption (XAS) pre-edge, and extended X-ray absorption fine structure (EXAFS) spectroscopies coupled with quantum chemical calculations have been correlated to the X-ray crystallographic structures. This has allowed the development of a detailed description of the geometric and electronic structure of the resting and substrate-bound site. The d → d transitions in the near-infrared spectral region are weak in absorption and masked by overtones of the buffer and protein. However, these transitions can be observed in CD and MCD spectroscopy and allow geometric and electronic structure information to be obtained from the experimental splitting of the ^5E_g and $^5T_{2g}$ states.[5,26] CD and MCD directly probe the ^5E_g splitting, and analysis of the VTVH MCD data provides the splitting of the $^5T_{2g}$ ground state.[5] Additionally, analysis of the 1s → 3d XAS pre-edge intensities and energy multiplet splittings provides complementary information on geometric and elec-

(8) Focht, D. D. *Curr. Opin. Biotechnol.* **1995**, *6*, 341−346.
(9) Mabrouk, P. A.; Orville, A. M.; Lipscomb, J. D. *J. Am. Chem. Soc.* **1991**, *113*, 4053−4061.
(10) Han, S.; Eltis, L. D.; Timmis, K. N.; Muchmore, S. W.; Bolin, J. T. *Science* **1995**, *270*, 976−980.
(11) Senda, T.; Sugiyama, K.; Narita, H.; Yamamoto, T.; Kimbara, K.; Fukuda, M.; Sato, M.; Yano, K.; Mitsui, Y. *J. Mol. Biol.* **1996**, *255*, 735−752.
(12) Uragami, Y.; Senda, T.; Sugimoto, K.; Sato, N.; Nagarajan, V.; Masai, E.; Fukuda, M.; Mitsui, Y. *J. Inorg. Biochem.* **2001**, *83*, 269−279.
(13) Kita, A.; Kita, S.; Fujisawa, I.; Inaka, K.; Ishida, T.; Horiike, K.; Nozaki, M.; Miki, K. *Structure* **1999**, *7*, 25−34.
(14) Sugimoto, K.; Senda, T.; Aoshima, H.; Masai, E.; Fukuda, M.; Mitsui, Y. *Structure* **1999**, *7*, 953−965.
(15) Davis, M. I.; Wasinger, E. C.; Westre, T. E.; Zaleski, J. M.; Orville, A. M.; Lipscomb, J. D.; Hedman, B.; Hodgson, K. O.; Solomon, E. I. *Inorg. Chem.* **1999**, *38*, 3676−3683.
(16) Hegg, E. L.; Que, L., Jr. *Eur. J. Biochem.* **1997**, *250*, 625−629.
(17) Que, L., Jr. *Nat. Struct. Biol.* **2000**, *7*, 182−184.
(18) Vaillancourt, F. H.; Barbosa, C. J.; Spiro, T. G.; Bolin, J. T.; Blades, M. W.; Turner, R. F. B.; Eltis, L. D. *J. Am. Chem. Soc.* **2002**, *124*, 2485−2496.
(19) Arciero, D. M.; Lipscomb, J. D.; Huynh, B. H.; Kent, T. A.; Munck, E. *J. Biol. Chem.* **1983**, *258*, 14981−14991.
(20) Bertini, I.; Briganti, F.; Mangani, S.; Nolting, H. F.; Scozzafava, A. *Biochemistry* **1994**, *33*, 10777−10784.
(21) Shu, L.; Chiou, Y.-M.; Orville, A. M.; Miller, M. A.; Lipscomb, J. D.; Que, L., Jr. *Biochemistry* **1995**, *34*, 6649−6659.
(22) Bull, C.; Ballou, D. P.; Otsuka, S. *J. Biol. Chem.* **1981**, *256*, 12681−12686.
(23) Hori, K.; Hashimoto, T.; Nozaki, M. *J. Biochem.* **1973**, *74*, 375−384.
(24) Nozaki, M.; Ono, K.; Nakazawa, T.; Kotani, S.; Hayaishi, O. *J. Biol. Chem.* **1968**, *243*, 2682−2690.
(25) Arciero, D. M.; Orville, A. M.; Lipscomb, J. D. *J. Biol. Chem.* **1985**, *260*, 14035−14044.
(26) Solomon, E. I.; Pavel, E. G.; Loeb, K. E.; Campochiaro, C. *Coord. Chem. Rev.* **1995**, *144*, 369−460.
(27) Westre, T. E.; Kennepohl, P.; DeWitt, J. G.; Hedman, B.; Hodgson, K. O.; Solomon, E. I. *J. Am. Chem. Soc.* **1997**, *119*, 6297−6314.
(28) Nerdinger, S.; Kendall, C.; Marchhart, R.; Riebel, P.; Johnson, M. R.; Yin, C.-F.; Eltis, L. D.; Sniekus, V. *Chem. Commun.* **1999**, 2259−2260.
(29) Vaillancourt, F. H.; Han, S.; Fortin, P. D.; Bolin, J. T.; Eltis, L. D. *J. Biol. Chem.* **1998**, *273*, 34887−34895.
(30) Bradford, M. M. *Biochemistry* **1976**, *15*, 248−254.
(31) Haigler, B. E.; Gibson, D. T. *J. Bacteriol.* **1993**, *172*, 457−464.

tronic structure,[27] and EXAFS provides accurate bond lengths and insight into the nature of the ligands. This combination of spectroscopic methods is used to evaluate quantum chemical calculations to obtain insight into the relative lack of dioxygen reactivity of the resting enzyme and its enhancement upon substrate binding.

Experimental Section

Sample Preparation. (1) Chemicals. Catechol and 3-methylcatechol were from Sigma-Aldrich (Mississauga, Ontario, Canada). 3-Methylcatechol was further purified by sublimation. Deuterium oxide (99.9 atom % D), *tert*-butyl alcohol-OD (99 atom % D), ethanol-OD (99 atom % D), and glycerol-$(OD)_3$ (98 atom % D) were from Cambridge Isotope Laboratories (Andover, MA) or from C/D/N Isotopes (Montreal, Quebec, Canada) and were used to eliminate the hydroxide overtones that dominate the IR absorption spectrum above 1600 nm. 2,3-Dihydroxybiphenyl,[28] 3-chlorocatechol, and 3-nitrocatechol were gifts from Dr. Victor Snieckus (Department of Chemistry, Queens University, Kingston, Ontario, Canada). Ferene-S was from ICN Biomedicals Inc. (Aurora, OH). All other chemicals were of analytical grade and used without further purification.

(2) Protein Purification. DHBD was anaerobically purified via anion-exchange and gel filtration chromatography and flash frozen in liquid nitrogen for long-term storage essentially as described previously.[29] In some cases, hydrophobic chromatography was performed between the anion-exchange and gel filtration steps to remove a minor heme-containing contaminant. This additional step was performed using a Source-15-phenyl column (Amersham Pharmacia Biosciences, Montreal, Quebec, Canada; 2 × 9 cm) equilibrated with 10 mM potassium phosphate, pH 7.0, containing 2 mM dithiothreitol and 0.5 M $(NH_4)_2SO_4$. Prior to loading, the protein sample was exchanged into this buffer using an Amicon ultrafiltration cell (Millipore Corporation, Bedford, MA). The column was operated at a flow rate of 15 mL/min, and DHBD eluted at approximately 0.3 M $(NH_4)_2SO_4$ using a linear gradient of 0.5 to 0 M $(NH_4)_2SO_4$ in 210 mL. The protein sample was exchanged into 10 mM Tris, 150 mM NaCl, pH 7.5, and the standard procedure[29] on Superdex column was performed in 10 mM Tris, 150 mM NaCl, pH 7.5 containing 10% *tert*-butyl alcohol, 2 mM dithiothreitol, and 0.25 mM ferrous ammonium sulfate. Preparations had a high specific activity (400−500 U/mg).

(3) Protein Sample Preparation. Samples were prepared under an inert atmosphere in an Mbraun Labmaster 100 glovebox (Stratham, NH) maintained at less than 1 ppm O_2. Buffers and solvents were vigorously bubbled with argon for 20 min, brought into the glovebox, and allowed to equilibrate for 24 h prior to use. Catecholic substrates were weighed in small glass vials (Wheaton, Millville, NJ) and transferred to the glovebox for sample preparation. For CD and MCD samples, aliquots of DHBD (1 to 2 mL) were transferred to the glovebox, thawed immediately prior to use, and exchanged into 20 mM HEPES, 80 mM NaCl, pD 8.0 ($I = 0.1$) or 20 mM HEPES, 80 mM NaCl, pD 7.0 ($I = 0.1$), containing 2 mM dithiothreitol and 10% *tert*-butyl alcohol-OD by gel filtration chromatography using a 1.5 cm × 8 cm column of Biogel P6 DG (Bio-Rad, Mississauga, Ontario, Canada). The protein was concentrated to 60−80 mg/mL using a 3 mL Amicon ultrafiltration cell equipped with a YM10 membrane (Millipore Corp.). Glycerol-$(OD)_3$ was then slowly added to a final concentration of 50−60%, and the sample was further concentrated to the desired protein concentration. CD spectra were taken with and without glycerol present to ensure that the site was unaffected by the glassing agent. Samples of the enzyme substrate complex were prepared by adding a minimum of a 5-fold excess of the catecholic substrate, prepared as a stock in ethanol-OD. Some DHBD samples also contained 10 μM sodium hydrosulfite. Samples were transferred to the appropriate sealed cuvettes or storage tube, removed from the glovebox, and flash frozen in liquid nitrogen. Protein concentrations were determined by the Bradford method.[30] Iron concentrations were determined colorimetrically using Ferene S.[31] Enzymatic activity was measured using a polarographic assay as described previously.[29] For X-ray absorption samples, CHBD was prepared at pH 8.0 using the same protocol except that the buffer and additives were not deuterated. The iron concentration of the samples was 0.3−1.8 mM for the UV−visible CD/MCD, 1.6−1.8 mM for the near-IR CD/MCD, and 1.7−2.0 mM for the X-ray absorption.

CD and MCD Spectroscopy. The near-IR data were collected on a Jasco J-200D (600−2140 nm) spectropolarimeter with a liquid N_2-cooled InSb detector. The J-200D is equipped with an Oxford Instruments SM4000-7 Tesla (T) superconducting magnet/cryostat capable of fields up to 7 T and temperatures down to 1.5 K. The UV/visible data were collected on a Jasco J-500C (200−1060 nm) with an extended S-20 and S-1 photomultiplier tube (Hammamatsu). The J-500C is equipped with an Oxford Instruments SM4-7 T superconducting magnet/cryostat capable of fields up to 7 T and temperatures down to 1.5 K.

CD samples were prepared in a 1 cm path length cuvette and were kept at 4 °C at all times with a circulating cooling bath attached to the sample holder. Buffer and cell baselines were subtracted from the raw protein CD spectra. Low temperature (1.6−50.2 K) MCD spectra were obtained in a copper MCD sample cell with two Infrasil quartz disks sandwiching a three mm thick neoprene O-ring spacer into which the sample was injected. MCD samples were rapidly frozen in liquid N_2 immediately after preparation. The depolarization of the frozen MCD sample, checked by measuring the CD spectrum of a nickel (+)-tartrate solution placed before and after the sample, was less than 5%.[32]

The MCD spectra were corrected for the natural CD and zero-field baseline effects caused by strain in the glasses by subtracting the 0 T scan from each of the other field scans at a given temperature. The CD and MCD spectra were iteratively fit to Gaussian band shapes by using a modified Levenberg−Marquardt constrained least-squares fitting routine. For VTVH MCD spectroscopy, a calibrated Cernox resistor (Lakeshore Cryotronics, calibrated 1.5−300 K) inserted in the sample cell was used to accurately measure the temperature of the sample. VTVH data were normalized to the maximum observed intensity and fit to an orientation-averaged intensity expression which includes rhombic and Zeeman splitting of a non-Kramers doublet, as well as the transition polarization ratio and contributions from linear temperature-independent B-terms and low-lying excited states.[26,33] Data were fit to both positive and negative zero-field splitting (ZFS) models to determine the best fit as discussed elsewhere.[34]

X-ray Absorption Spectroscopy. Samples for the XAS experiments were transferred into a Lucite XAS cell with 37 μM windows and frozen in liquid nitrogen. An EPR spectrum was recorded to ensure the lack of a ferric signal. X-ray absorption spectra were measured at the Stanford Synchrotron Radiation Laboratory (SSRL) on beam line 9-3 under standard conditions of 3 GeV and 50−100 mA. The beam line utilized a Rh-coated harmonic rejection and collimation mirror, set to a cutoff of 11 keV, a Si(220) double-crystal monochromator (fully tuned), and a cylindrical bent focusing Rh-coated mirror. Data were obtained to $k = 17$ Å^{-1}. A constant sample temperature of 10 K was maintained using an Oxford Instruments liquid helium CF1208 cryostat. Each scan was internally calibrated using an iron foil, assigning the first inflection point to 7111.2 eV.[35] The spectrometer energy resolution was better than 1.4 eV with reproducibility in edge position of <0.2 eV. Fluorescence data monitoring the Fe Kα fluorescence signal were measured using a 30-element Ge solid-state array detector with a three-wavelength Mn filter and Soller slits aligned between the detector and

(32) Browett, W. R.; Fucaloro, A. F.; Morgan, T. V.; Stephens, P. J. *J. Am. Chem. Soc.* **1983**, *105*, 1868−1872.
(33) Pavel, E. G.; Kitajima, N.; Solomon, E. I. *J. Am. Chem. Soc.* **1998**, *120*, 3949−3962.
(34) Campochiaro, C.; Pavel, E. G.; Solomon, E. I. *Inorg. Chem.* **1995**, *34*, 4669−4675.
(35) Scott, R. A.; Hahn, J. E.; Doniach, S.; Freeman, H. C.; Hodgson, K. O. *J. Am. Chem. Soc.* **1982**, *104*, 5364−5369.

the sample to improve the ratio of usable Fe Kα fluorescence signal to that of scattered beam.[36]

EXAFS data reduction was performed on the averaged protein data according to established methods.[37−39] A smooth pre-edge background was removed from the spectrum by fitting a Gaussian polynomial to the pre-edge region and subtracting this polynomial from the entire spectrum. A spline through the EXAFS region was chosen so that it minimized residual low-frequency background but did not reduce the EXAFS amplitude as checked by monitoring the Fourier transform of the EXAFS during the background subtraction process, and the data were normalized. The normalized data were converted to *k*-space, where the photoelectron wave vector, *k*, is defined by $[2m_e(E - E_o)\hbar^2]^{1/2}$, where m_e is the electron mass, *E* is the photon energy, $\hbar$ is Planck's constant divided by 2π, and E_o is the threshold energy of the absorption edge, which was defined to be 7130 eV for the Fe K absorption edge.

Theoretical EXAFS signals $\chi(k)$ were calculated using FEFF (version 6) and fit to the data using EXAFSPAK (Dr. G. N. George, SSRL). The structural parameters varied were *R*, the bond distance; σ^2, the bond variance; and E_0, the threshold ($k = 0$ point) shift in eV. The bond variance is related to the Debye−Waller factor, which is a measure of the thermal vibration and static disorder of the absorber−scatterer pair. Although the threshold energy E_0 was allowed to vary in each fit, it was restricted to a common value for every component in that fit. Coordination numbers were systematically varied in the course of the analysis, but were not allowed to vary within a fit. For the first coordination sphere, the total coordination number was restricted to that resulting from XAS pre-edge analysis (vide infra). Fits were evaluated by comparing the normalized error for the fits, calculated as the sum of the squares of the differences between experimental and calculated curves.

The intensities and energies of the pre-edge features of the protein data were quantified with the fitting program EDG_FIT (Dr. G. N. George, SSRL) that utilizes the double precision version of the public domain MINPAK fitting library. All spectra were fit over the range 7108−7118 eV. Pseudo-Voigt line shapes of a fixed 50:50 ratio of Lorentzian to Gaussian contribution were used to model pre-edge features and successfully reproduced the spectra. Functions modeling the background contributions to the pre-edge features were chosen empirically to give the best fit and included pseudo-Voigt functions that mimicked shoulders on the rising edge. For all complexes, 8−10 fits were obtained which equally well reproduced the data and the second derivative with variation in the background function used. A fit was considered acceptable only if it successfully reproduced the data and the second derivative of the data. The values reported for the areas of the pre-edge features, where peak area is approximated by the height multiplied by the full-width-at-half-maximum, are the average of all the pseudo-Voigt functions that successfully fit the feature and its second derivative. To quantify the error, the standard deviations for the peak energies and intensities were calculated from all of the pseudo-Voigt functions that fit the pre-edge features from all of the successful fits for each sample.

Electronic Structure Calculations. (1) Active Site Geometry. The active site geometric structure was obtained from the crystallographic coordinates of DHBD (PDB ID: 1HAN)[10] (as depicted in Scheme 1) with the ligand−metal bond lengths modified by EXAFS results (vide infra). Hydrogen atoms were placed at standard bond lengths and angles. The hydrogen atoms on the two water ligands for resting DHBD were placed in the minimum energy conformation from a Hartree−Fock level minimization routine using INDO/S-CI.[40] The following model was used for the calculations on DHBD: two water ligands, imidazoles to model the two histidines, and formate to model the glutamate residue. For the DHBD-DHB complex, in addition to the two imidazoles, formate, and a single water, the substrate was modeled by a monoanionic catecholate. All other internal coordinates were left unchanged. The EXAFS bond lengths for DHBD-DHB are 2.13 Å for the histidines, 1.98 Å for glutamate, and 1.98 and 2.52 Å for the deprotonated and protonated Fe−substrate bonds, respectively. Cartesian coordinates of the models (with Fe at the origin) used in the calculations are included as Supporting Information (Table S1).

(2) DFT Calculations. The Amsterdam density functional (ADF 2.0.1) program developed by Baerends et al. was used for the single point calculations of DHBD and DHBD-DHB for comparison with the spectroscopic results.[41,42] The calculations were performed on an SGI workstation. The local density approximation (LDA) of Vosko and coworkers was used,[43] together with the gradient corrections of Becke for the exchange[44] and of Perdew for the correlation (BP86).[45] The calculations were spin-polarized with an uncontracted triple-ζ basis set (ADF basis set IV) with a single polarization function used for all atoms. Core orbitals were frozen through 1s (C, N, O) and 3p (Fe). Calculations were accepted as converged when the maximum element in the error matrix, which is defined as the commutator of the Fock matrix and the density matrix, was less than 10^{-5}. Graphical output of the computational results was generated with the Cerius^2 software program (Molecular Simulations, Inc.).

Spin-unrestricted DFT calculations were performed to study the thermodynamics of the reaction of O_2 with DHBD using Becke's three-parameter hybrid functional with the correlation function of Lee, Yang, and Parr (B3LYP)[46−48] as well as Becke's 1988 exchange functional with the correlation function of Perdew (BP86).[44,45] Computations were carried out with the program package Gaussian 98 (G98).[49]

Two sets of models were used for the DHBD and DHBD-O_2 complexes. A simplified model, comprised of two water ligands, two ammonias (NH_3) (in place of histidine ligands), and one formate (HCO_2^-) ligand (in place of the glutamate ligand), was fully optimized without constraints. An extended model including two water ligands, two Me-imidazoles, and one acetate ligand was partially optimized with the distances between the β-carbons of the backbone held constant. [A full optimization of the 5C DHBD extended model with the partially optimized structure as a starting point did not show any significant changes in electronic and geometric structure, or in the energetics. The fully optimized structure is in agreement with the DHBD model optimized on a HF-level by Kraus.[50]] Both models were optimized with the LanL2DZ[51−54] basis set, and frequencies as well as thermodynamic parameters were calculated. The frequencies were found to be real in all cases. For the calculation of reaction energies, an all electron triple-ζ valence basis set (TZV; used as implemented in the G98 program

(36) Cramer, S. P.; Tench, O.; Yocum, M.; George, G. N. *Nucl. Instrum. Methods Phys. Res.* **1988**, *A266*, 586.
(37) Cramer, S. P.; Hodgson, K. O. *Prog. Inorg. Chem.* **1979**, *25*, 1−39.
(38) Cramer, S. P.; Hodgson, K. O.; Stiefel, E. I.; Newton, W. E. *J. Am. Chem. Soc.* **1978**, *100*, 2748−2761.
(39) Scott, R. A. *Methods Enzymol.* **1985**, *117*, 414−459.
(40) Neese, F. Using the program ORCA2000 developed by Frank Neese.
(41) Baerends, E. J.; Ellis, D. E.; Ros, P. *Chem. Phys.* **1973**, *2*, 41−51.
(42) Velde, G. t.; Baerends, E. J. *J. Comput. Phys.* **1992**, *99*, 84−98.
(43) Vosko, S. H.; Wilk, L.; Nusair, M. *Can. J. Phys.* **1980**, *58*, 1200−1211.
(44) Becke, A. D. *Chem. Phys.* **1986**, *84*, 4524−4529.
(45) Perdew, J. P. *Phys. Rev. B* **1986**, *33*, 8822−8824.
(46) Becke, A. D. *Phys. Rev. A* **1988**, *38*, 3098−3100.
(47) Becke, A. D. *J. Chem. Phys.* **1993**, *98*, 1372−1377.
(48) Becke, A. D. *J. Chem. Phys.* **1993**, *98*, 5648−5652.
(49) Frisch, M. J. T., G. W.; Schlegel, H. B.; Scuseria, G. E.; Robb, M. A.; Cheeseman, J. R.; Zakrzewski, J. A.; Montgomery, J. A.; Stratman, R. E.; Burant, J. C.; Dapprich, J. M.; Millam, J. M.; Daniels, A. D.; Kudin, K. N.; Strain, M. C.; Farkas, O.; Tomasi, J.; Barone, V. C. M.; Cammi, R.; Mennucci, B.; Pomelli, C.; Adamo, C.; Clifford, S.; Ochterski, J.; Peterson, G. A.; Ayala, P. Y.; Cui, Q.; Morokuma, K.; Malick, D. A.; Rabuck, A. D.; Raghavachari, K.; Foresman, J. B.; Cioslowski, J.; Ortiz, J. V.; Stefanov, B. B.; Liu, G.; Liashenko, A.; Piskorz, P.; Komaromi, I.; Gomperts, R.; Martin, R. L.; Fox, D. J.; Keith, T.; Al-Laham, M. A.; Peng, C. Y.; Nanayakkara, A.; Gonzalez, C.; Challacombe, M.; Challacombe, M.; Gill, P. M. W.; Johnson, B. G.; Chen, W.; Wong, M. W.; Andres, J. L.; Head-Gordon, M.; Replogle, E. S.; Pople, J. A. *Gaussian 98*; Gaussian, Inc.: Pittsburgh, PA, 1998.
(50) Kraus, M. *Int. J. Quantum Chem.* **2000**, *76*, 331−340.
(51) Dunning, T. H., Jr.; Hay, P. J. In *Modern Theoretical Chemistry*, 3rd ed.; Schaefer, H. F., Ed.; Plenum: New York, 1976.
(52) Hay, P. J.; Wadt, W. R. *J. Chem. Phys.* **1985**, *82*, 270−283.
(53) Hay, P. J.; Wadt, W. R. *J. Chem. Phys.* **1985**, *82*, 299−310.
(54) Wadt, W. R.; Hay, P. J. *J. Chem. Phys.* **1985**, *82*, 284−298.

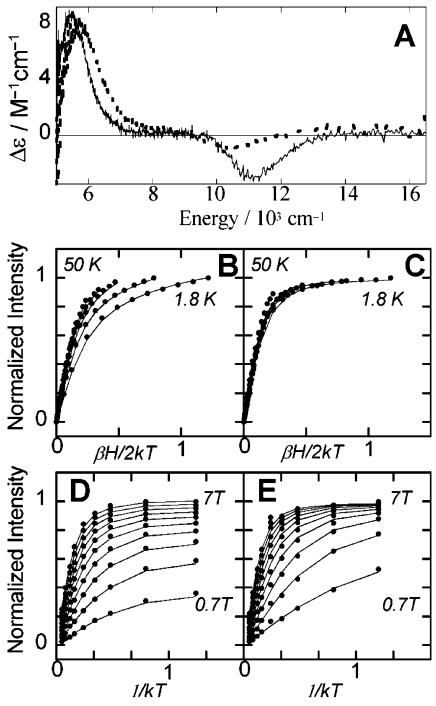

Figure 1. (A) MCD spectra at 5 K and 7 T of DHBD (−) and the DHBD-DHB (- - -). (B) VTVH saturation magnetization behavior recorded at 5525 cm^{-1} for DHBD and at (C) 6330 cm^{-1} for DHBD-DHB where the normalized data (●) and fit (−) of the data are plotted vs $\beta H/2kT$ for a series of fixed temperatures (1.8, 3.0, 4.9, 6.9, 10.0, 15.1, 20.2, 30.0, and 50.2 K). The data and fit are replotted for (D) DHBD and (E) DHBD-DHB as a function of $1/kT$ for a series of fixed fields (0.7, 1.4, 2.1, 2.8, 3.5, 4.2, 4.9, 5.6, 6.3, 7.0 T; 0.35 T omitted for clarity). The standard deviations in the data points are approximately the size of the symbol used and have been omitted for clarity.

package) of Ahlrichs and co-workers[55] was applied on the LanL2DZ-optimized structures. Solvation effects were included in the calculations using the polarized continuum model (PCM)[56] and a dielectric constant $\epsilon = 4.0$ to model the protein environment. In all calculations, convergence was reached when the relative change in the density matrix between subsequent iterations was less then 1×10^{-8}.

Results and Analysis

CD and Low-Temperature MCD Spectroscopy. Near-IR low-temperature MCD spectra (Figure 1A) were measured for high-spin ferrous DHBD (−) and DHBD-DHB (- - -). CD spectra taken with and without the glassing agent glycerol present were found to be unchanged. The spectrum of DHBD was unchanged upon varying the pH from 8.0 to 7.0.

There are two bands present, at 5500 and 11 000 cm^{-1} for DHBD and at 6000 and 10 500 cm^{-1} for DHBD-DHB. Perturbations to the substrate were also explored where the phenyl substituent was replaced with methyl, chloro, and nitro groups. The d → d transitions vary as given in Table 1. The trend inversely follows the Hammet series (nitro > chloro > phenyl ≈ methyl) with the energy increasing through the series due to stronger donor bonding with less electron-withdrawing substituents. In addition to the low energy d → d transitions, at higher energy the substrate complexes exhibit the onset of an intense charge-transfer transition that is sensitive to the nature of the substrate substituents as shown in Table 1, band 3. It is

Table 1. MCD Transition Energies for DHBD and DHBD with Various Substrates

sample[a]	band 1[b]	band 2[b]	band 3[b,c]
DHBD	5500	11 000	
DHBD-DHB	6000	10 500	28 000
DHBD-(meth-cat)	5470	10 430	31 000
DHBD-(cl-cat)	5310	10 320	31 000
DHBD-NO_2cat	∼5100	10 100	ND

[a] The substrates have the phenyl group of DHB replaced by methyl, chloro, and nitro groups, respectively. [b] All units in cm^{-1}. [c] This marks the onset of the high energy band because the maximum is too high in energy to be resolved here. ND = not able to be determined due to intense CT from the free substrate itself that interferes in this region.

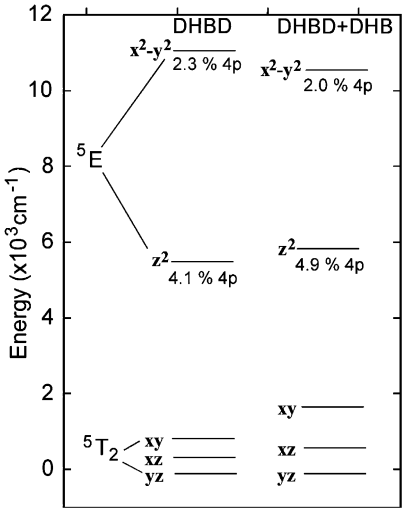

Figure 2. Experimentally derived d-orbital splitting pattern for DHBD and DHBD-DHB from CD and MCD spectroscopy.

interesting to note the presence of a negative band 2 in the MCD spectrum in Figure 1 for both of these systems because most square pyramidal model complexes and other ferrous enzyme systems have all positive low-temperature MCD bands.[5,33]

Information about the geometric and electronic structure of the active site can be obtained from an analysis of the energies and splitting pattern of MCD bands. The ^5D ground state for the high spin Fe(II) (d^6) free ion is split in octahedral symmetry into a triply degenerate $^5T_{2g}$ ground state and a doubly degenerate ^5E_g excited state separated by 10 Dq (∼10 000 cm^{-1} for biologically relevant nitrogen and oxygen ligands). In the low symmetry of the protein site, both of these states split in energy where the splitting of the ^5E_g state directly represents the splitting of the e_g orbitals ($d_{x^2-y^2}$ and d_{z^2}), and the splitting of the $^5T_{2g}$ state reflects the splitting on the t_{2g} orbitals (d_{xz}, d_{yz}, and d_{xy}). This leads to two d → d transitions centered at 10 000 cm^{-1}, split by ∼2000 cm^{-1} for a six-coordinate site.[26] Removal of a ligand leads to a five-coordinate square pyramidal site resulting in two transitions, one at ∼5000 cm^{-1} and one >10 000 cm^{-1}.[26] Rearrangement to a trigonal bipyramidal site leads to one transition at <10 000 cm^{-1} and one at <5000 cm^{-1}.[26] A four-coordinate ferrous site has a much smaller value of 10 Dq (10 $Dq(T_d) = -(4/9)10Dq(O_h)$), and thus only low energy transitions are observed (5000−7000 cm^{-1}).[26] The experimental d-orbital splittings for DHBD and DHBD-DHB obtained from the MCD and VTVH MCD data (vide infra) are shown in Figure 2. The observed MCD splitting ($\Delta^5E_g = 5500$ cm^{-1}) and the energies of these two d → d transitions in DHBD are consistent with a five-coordinate square pyramidal active

(55) Schäfer, A.; Huber, C.; Ahlrichs, R. *J. Chem. Phys.* **1994**, *100*, 5829−5835.
(56) Cramer, C. J.; Truhlar, D. G. *Chem. Rev.* **1999**, *99*, 2161−2200.

site. The MCD splitting ($\Delta^5E_g = 4500$ cm^{-1}) and the energies of the two bands in DHBD-DHB also indicate a five-coordinate square pyramidal active site which is different from that in DHBD. The decrease in Δ^5E_g for DHBD-DHB would be consistent with a stronger axial direction shifting the Fe(II) out of the equatorial plane, thus raising the energy of the d_{z^2} orbital and lowering the energy of the $d_{x^2-y^2}$ orbital.

VTVH MCD Spectroscopy. The VTVH data, collected at a variety of temperatures and fields, for the DHBD d → d transition at 5525 cm^{-1} (same as the data at 11 110 cm^{-1}, not shown) and the DHBD-DHB d → d transition at 6010 cm^{-1} (same as the data at 10 420 cm^{-1}, not shown), were normalized and plotted as a function of $\beta H/2kT$ (Figure 1B and 1C, respectively) and $1/kT$ (Figure 1D and 1E, respectively) (where β is the Bohr magneton and k is the Boltzmann constant) to separate the effects of temperature and field.

The VTVH MCD data for DHBD-DHB relative to DHBD are much less nested (i.e., less spread out) when plotted versus $\beta H/2kT$. The increase in MCD intensity with decreasing temperature shown in Figures 1B and 1C is indicative of *C*-term behavior in the negative zero-field splitting (ZFS) case or a temperature-dependent *B*-term intensity mechanism in the positive ZFS case.[26,34] The VTVH MCD data for both DHBD and DHBD-DHB are best fit by a negative ZFS non-Kramers doublet model. Negative ZFS splitting of the $S = 2$ manifold leads to $M_s = \pm 2$, ± 1, 0 levels split by $3D$ and D, respectively, where the lowest doublet ($M_s = \pm 2$) is further split by the rhombic distortion δ which causes the wave functions to mix. When a magnetic field is applied, the $M_s = \pm 2$ components are further split by an amount $g_{\|}\beta H$ and the wave functions change to become pure $|+2\rangle$ and $|-2\rangle$ at high field. This change in wave function composition as a function of field leads to the nesting of the data (Figure 1B and 1C) and to the differences in signal amplitudes between the curves taken at different fields in the low-temperature region in the $1/kT$ plots (Figure 1D and 1E). The ground-state spin-Hamiltonian parameters, δ, $g_{\|}$, can be extracted from the VTVH data (see ref 28 for details), which in turn give the axial and rhombic splittings of the $^5T_{2g}$ orbitals, Δ ($\Delta = d_{xz,yz} - d_{xy}$) and V ($V = d_{xz} - d_{yz}$). The best fit to DHBD has $\delta = 4.2 \pm 0.2$ cm^{-1}, $g_{\|} = 8.8$, and an excited singlet sublevel energy of ~23 cm^{-1}. This corresponds to $\Delta = -700$ cm^{-1} and $V = 450$ cm^{-1}, and $\Delta^5T_{2g} = 925$ cm^{-1} (where $\Delta^5T_{2g} = \Delta + |V|/2$). The best fit to DHBD-DHB has $\delta = 2.0 \pm 0.2$ cm^{-1}, $g_{\|} = 8.8$, and an excited singlet sublevel energy of ~18 cm^{-1} corresponding to $\Delta = -1200$ cm^{-1}, $V = 700$ cm^{-1}, and $\Delta^5T_{2g} = 1550$ cm^{-1}. The smaller value of δ (which is also observed for all of the other substrate-active site complexes studied here, not shown) indicates a larger $^5T_{2g}$ splitting (bottom of Figure 2), reflecting the stronger π donation in DHBD-DHB. Additionally, the sign of D (negative) indicates that the square pyramidal site has a weak axial direction.[26] These values of Δ and V combined with the many electron spin−orbital coupling parameter (λ) of −80 cm^{-1} were used to calculate the percent mixing of the three t_{2g} orbitals from the $^5T_{2g}$ Hamiltonian (eq 9 in ref 5). For both DHBD and DHBD-DHB, each of the three t_{2g} d-orbitals is over 90% pure, as the spin−orbit coupling is small relative to the ligand field energy splitting of the t_{2g} set of d orbitals.

X-ray Absorption Spectroscopy: Pre-edge. Model studies have shown that pre-edge shape and intensity patterns can be related to coordination number and geometry.[27] The 1s → 3d pre-edge features are formally electric dipole forbidden, but gain intensity through an electric quadrupole mechanism, and are therefore weak in centrosymmetric complexes. Six-coordinate ferrous complexes have a total pre-edge intensity of ~3.9 units with a pre-edge shape consisting of three features spread over approximately 2.3 eV.[27] In contrast, five- and four-coordinate ferrous models typically have two features with a higher total pre-edge intensity of ~12 units.[27] The removal of one or two ligands in five-coordinate or tetrahedral model complexes, respectively, leads to the strong loss of inversion and significant 4p orbital mixing into the unoccupied 3d orbitals. Because the 1s → 4p electric dipole allowed transition is ~100-fold more efficient than the quadrupole transition, a few percent 4p mixing greatly enhances the intensity of the pre-edge feature.

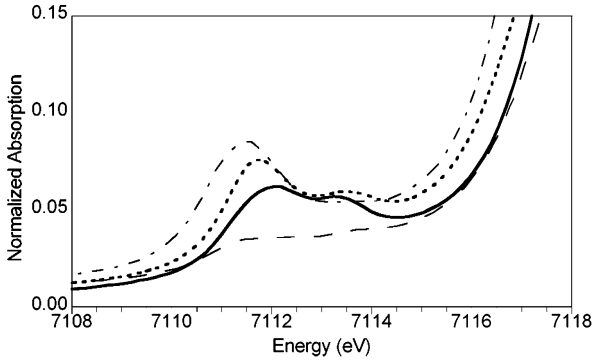

Figure 3. XAS pre-edge of ferrous DHBD (−), DHBD-DHB (- - -), the five-coordinate model complex $[Fe(TMC)Cl]^+$ (- −), and the six-coordinate model complex $[Fe(imidazole)_6]Cl_2$ (− − −).

Table 2. Pre-edge Intensity Distribution of Ferrous DHBD and DHBD-DHB and Ferrous Model Complexes[a]

	energy (eV)	area	energy (eV)	area	energy (eV)	area	total
DHBD	7111.9	7.7(0.7)	7113.3	3.8(0.5)			11.7(0.3)
DHBD-DHB	7111.7	8.9(0.7)	7113.6	3.4(0.4)			12.3(0.6)
$[FeCl_4]^{2-}$	7111.6	8.6(0.4)	7113.1	4.3(0.7)			12.9(0.6)
$[Fe(TMC)Cl]^{1+}$	7111.4	10.9(0.1)	7113.2	2.0(0.3)			12.9(0.2)
$[Fe(H_2O)_6]^{2+}$	7111.3	2.2(0.5)	7112.3	0.7(0.3)	7113.6	1.1(0.3)	4.9(0.5)

[a] Standard errors are presented in parentheses.

The pre-edge spectra of ferrous DHBD without and with substrate are shown in Figure 3, along with representative spectra of a five- and a six-coordinate model complex.[27]

The pre-edge of each sample is clearly comprised of two features. This parallels the intensity distribution of four- and five-coordinate model complexes. The individual peak energies and areas used to fit the pre-edge features of DHBD and DHBD-DHB are listed in Table 2, along with those of the ferrous model complexes. The total pre-edge area for DHBD of 11.7 units is similar to that of four- and five-coordinate model complexes and much greater than that found for octahedral ferrous complexes. Similarly, the pre-edge area of DHBD-DHB is 12.3 units, comparable to four- and five-coordinate model complexes.

A ligand field multiplet analysis for a square pyramidal system provides an understanding of the intensity distribution in the two DHBD complexes. The C_{4v} ligand field around the iron removes the degeneracy of the 3d orbitals (Scheme 2) and causes the ^4F and ^4P $d^{(n+1)}$ free ion ground states to split into seven many-electron excited states ($^4A_2$,$^4B_1$, ^4E, $^4B_2$, and ^4E, and $^4A_2$ and ^4E, respectively).

Scheme 2

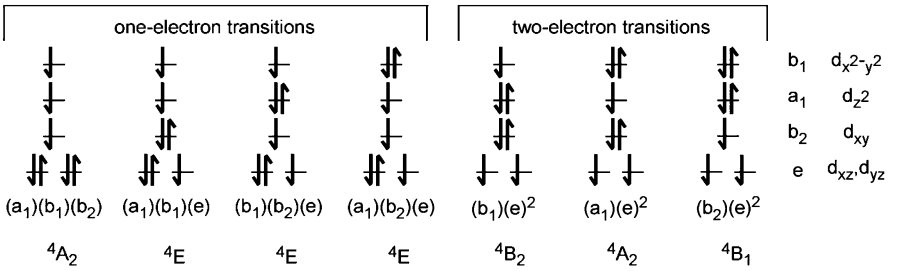

Linear combinations of the (e)(a_1)(b_1), (e)(b_2)(b_1), and (e)(b_2)(a_1) hole configurations give rise to the three ^{4}E states, while the (b_2)(a_1)(b_1) and (e)^2(a_1) hole configurations give rise to two $^4A_2$ states. The $^4B_2$ and $^4B_1$ states arise from the (b_1)(e)^2 and (b_2)(e)^2 hole configurations, respectively. Coupling the $^2A_1$ core hole to the d$^{(n+1)}$ quartet states results in a series of triplet and quintet final states. For a high-spin $S = 2$ ferrous ground-state ion, only transitions to the quintet states are spin allowed. Furthermore, only excited states with one-electron transition character will have appreciable pre-edge intensity. The $^5B_2$ and $^5B_1$ final states, which arise from two-electron transitions (from the (e)^3(a_1)^1 and (b_1)^1(b_2)^1 ground configurations), are not of the appropriate symmetry to mix with any of the one-electron allowed states and therefore will not contribute to the pre-edge spectra. Additionally, because the two $^5A_2$ final states are allowed to mix by group theory, both $^5A_2$ states may have some one-electron allowed character. Thus, only the two $^5A_2$ final states and the three ^{5}E final states need to be considered in the pre-edge analysis.

The electric quadrupole intensity is distributed among these five quintet final states according to the degeneracy of the state and the percentage of the one-electron allowed strong field component for the $^5A_2$ states. The large energy splitting of the two $^5A_2$ states, however, indicates that little quadrupole character will be transferred to the higher state through configuration interaction (CI) mixing, and thus to first order the quadrupole intensity of the $^5A_2$:^{5}E:^{5}E:^{5}E:$^5A_2$ is 1:2:2:2:0. The pre-edge features of DHBD should also gain intensity through the electric dipole mechanism involving 4p mixing into the d-manifold. Because of the lack of a ligand in the axial direction, mixing of the 4p$_z$ orbital with the d$_{z^2}$ orbital, which contributes to the ^{5}E state from the (b_1)(b_2)(e) configuration, is expected to dominate the electric dipole contribution for a C_{4v} complex. However, from the ferrous DHBD crystal structure, the glutamate ligand is in the equatorial position, and EXAFS analysis (vide infra) has identified a short ligand in the first coordination shell. Thus, 4p mixing along the direction of the short glutamate ligand is expected to also contribute for a transition into the d$_{x^2-y^2}$ orbital and thus mix electric dipole intensity into the highest energy ^{5}E state ((a_1)(b_2)(e) configuration), although to a lesser extent than 4p$_z$ mixing into the d$_{z^2}$ orbital. The three ^{5}E many-electron excited states are allowed to mix by symmetry, and the dipolar intensity will be distributed into the other states according to the amount of one-electron transition character to the d$_{z^2}$ and d$_{x^2-y^2}$ orbitals in the CI mixed ^{5}E states. Thus, the dipole intensity will reside primarily in the middle ^{5}E state, while a smaller amount resides in the highest energy ^{5}E. Finally, the iron atom is 0.23 Å out of the plane formed from minimizing the root-mean-square deviation of the best plane of the four equatorial ligands. The distortion allows mixing of the 4p$_{x,y}$ orbitals into the e(d$_{xz}$,d$_{yz}$) levels, and thus dipole character is expected to contribute to the low energy $^5A_2$ state to a limited extent.

In the case of ferrous DHBD-DHB, the glutamate ligand is in the axial direction. While the quadrupole intensity distribution is not significantly dependent on geometry, the electric dipole intensity is redistributed according to the directionality of the 4p mixing. With the short glutamate no longer in the equatorial direction, 4p mixing into the d$_{x^2-y^2}$ orbital is decreased, dipole intensity in the highest energy ^{5}E is greatly reduced, and a greater percentage of dipole intensity contributes to the middle energy ^{5}E state. Further, the greater ligand strength of the now axial glutamate ligand relative to the histidine axial ligand in the DHBD complex causes a greater distortion of the iron out of the plane of the equatorial ligands (0.26 Å versus 0.23 Å). This allows greater 4p mixing into the d$_{xz}$ and d$_{yz}$ orbitals that primarily contribute to the lower energy $^5A_2$ excited state. Therefore, the higher energy feature in the pre-edge spectrum is expected to decrease in amplitude, while the lower energy feature is expected to gain intensity relative to DHBD. This analysis is consistent with the observed XAS pre-edge data. Comparison of the intensity distribution for DHBD-DHB and DHBD reveals a shift in intensity to lower energy upon substrate binding (Figure 3); the low energy feature increases in intensity from 7.9 to 8.9 units, while the high energy feature loses intensity, going from 3.8 to 3.4 normalized units.

Ferrous octahedral model complexes have been shown to have pre-edge intensities of 3.1−4.4 units, with an average pre-edge intensity of 3.9 normalized units, reflecting a purely quadrupolar intensity mechanism.[27] If 3.9 units of intensity are attributed to the quadrupole mechanism in DHBD and DHBD-DHB, then 7.8 and 8.4 units of intensity must originate from the dipolar mechanism. A correlation has previously been developed for ferrous complexes relating 1% of 4p mixing to 1.22 (0.5) units of intensity.[27] Therefore, DHBD and DHBD-DHB are found to have 6.4% and 6.9% 4p character mixed into the d-manifold, respectively. This compares reasonably with DFT calculations (vide infra) that give 4.1% 4p character for DHBD and 5.7% in DHBD-DHB and with a shift of 4p mixing to increase p$_z$ in d$_{z^2}$.

X-ray Absorption Spectroscopy: EXAFS. The averaged EXAFS data for DHBD and DHBD-DHB are generally similar as shown in Figure 4A. Significant differences are observed, however, in the $k = 6-10$ Å^{-1} range. These differences can be seen more easily in the Fourier transforms of the data (Figure 4B). The main differences are in the appearance of a feature at ~2.0 Å and the elimination of a feature at ~2.6 Å (nonphase shift corrected) in the DHBD-DHB Fourier transform relative to that of DHBD.

Table 3. EXAFS Fits of Ferrous DHBD and DHBD-DHB

	DHBD									DHBD-DHB								
fit #:	1			2			3			4			5			6		
E_o:	−7.1			−7.1			−7.5			−8.9			−9.1			−10.8		
	CN	R (Å)	σ^2 (Å^2)[a]	CN	R (Å)	σ^2 (Å^2)[a]	CN	R (Å)	σ^2 (Å^2)[a]	CN	R (Å)	σ^2 (Å^2)[a]	CN	R (Å)	σ^2 (Å^2)[a]	CN	R (Å)	σ^2 (Å^2)[a]
Fe−O/N	0			1	1.98	129	2	2.01	326	1	1.96	44	2	1.98	230	2	1.98	196
Fe−O/N	5	2.08	823	4	2.12	546	3	2.15	424	4	2.10	603	3	2.14	393	2	2.13	178
Fe−O/N																1	2.52	580
$C_\alpha SS$[b]	8	3.08	943	5	3.08	924	5	3.08	948									
$C_\beta SS$[b]	4	3.19	582	4	3.23	1045	4	3.27	1231	6	3.44	512	6	3.44	522	6	3.44	479
$C_\beta MS$[b]	8	4.32	975	8	4.32	966	8	4.32	962	10	4.34	468	10	4.34	476	10	4.32	462
error (F)[c]		0.15			0.11			0.11			0.16			0.15			0.20	

[a] Values have been multiplied by 10^5 for convenience. [b] SS: single scattering. MS: multiple scattering. [c] $F = \Sigma[(\chi_{exp} - \chi_{obsd})^2 k^6]/\Sigma[\chi_{exp}^2 k^6]$.

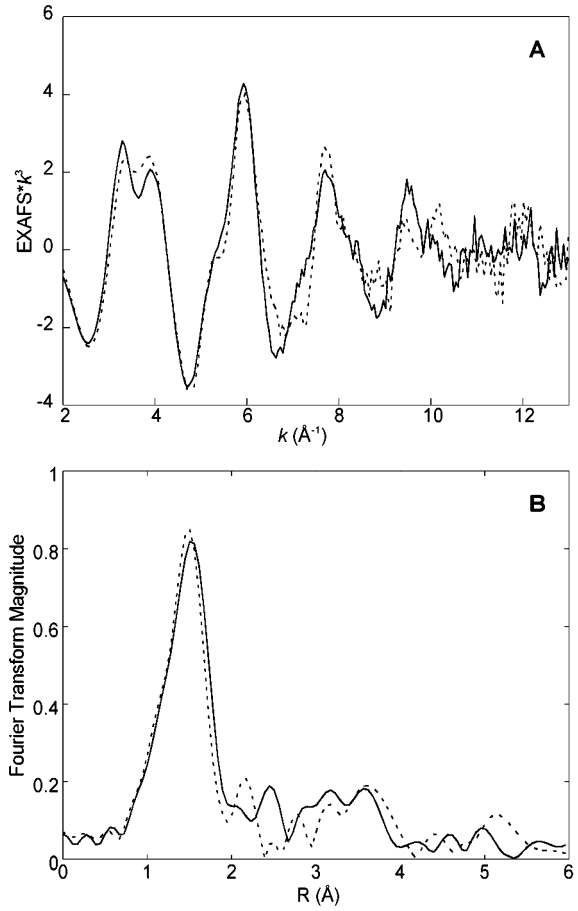

Figure 4. (A) EXAFS and (B) Fourier transforms of DHBD (−) and DHBD-DHB (- - -).

Fits to the EXAFS data of DHBD and DHBD-DHB are given in Table 3. All fits are restricted to five first-coordination shell ligands as required by the pre-edge and MCD analysis (vide supra). Two components are required to fit the first coordination sphere of DHBD. A single N/O ligand is found at 1.98 Å, and four additional N/O ligands are required at 2.12 Å (fit 2, Table 3). Attempting to fit the data with a single shell results in all five ligands at an average distance of 2.08 Å (fit 1). The fit quality decreases, however, as is observed in the increase in the error function (F).

Attempting to fit the data with two ligands at the short distance results in a statistically equivalent fit (Table 3, fit 3), while fitting with three ligands causes the Debye−Waller factor to become unreasonably large (not shown). Adding a single N/O at 0.10 Å intervals from 2.10 to 2.50 Å tested the possibility of a ligand at a distance longer than 2.10 Å. None of these fits were improved relative to that of fit 2, and in all cases the longest component was virtually eliminated by the resulting large Debye−Waller factor. The first coordination sphere of DHBD-DHB also requires two components: 2 N/O at 1.98 Å and 3 N/O at 2.14 Å (fit 5). Note that the distribution has shifted from 1:4 in DHBD to 2:3 in the DHBD-DHB complex. Attempting to fit the data of the substrate bound species with one short and four longer ligands (fit 4) results in a worse fit function value, a worse fit visually to the spectrum, and a Debye−Waller factor too low in the first component. A long third component can be included in the fit of DHBD-DHB at 2.52 Å (fit 6). This fit, however, is not improved relative to fit 5. Thus, the additional possible feature is not supported by the data, consistent with the recent five-coordinate DHBD-DHB structure. Finally, additional components representing the single and multiple scattering of the carbon atoms from the ligands are required and are listed with the respective fits in Table 3.

Density Functional Calculations. DFT electronic structure calculations were performed on DHBD and DHBD-DHB to correlate the spectroscopy to the known X-ray crystallography.[10,18,57] The calculations evaluate the experimental energy level diagram in Figure 2, probe the origin of the negative sign for the MCD intensity for the higher energy band 2 in Figure 1, and provide insight into the 4p mixing which can be compared to XAS pre-edge results. Additionally, DFT calculations supported by data were used to probe the origin of the low O_2 reactivity of the resting site.

(1) DHBD. For the calculations, a coordinate system was chosen with the axial histidine as z, the Fe-glutamate bond as x, and the y-direction most closely aligned with the equatorial histidine−iron bond. The ground-state orbital energies and one-electron wave functions from the DFT calculations are summarized in Table 4. The five spin-down d-orbitals (spin-unrestricted) are the highest occupied molecular orbital (contour in Figure 5 and #48 in Table 4) and the four lowest unoccupied orbitals.

The calculated splitting pattern $d_{x^2-y^2} > d_{z^2} > d_{xy} > d_{xz} > d_{yz}$ is consistent with experiment (Figure 2) and the approximate square pyramidal site structure from X-ray crystallography.[10] The least amount of metal character is in the $d_{x^2-y^2}$ orbital which

(57) Sato, N.; Uragami, Y.; Nishizaki, T.; Takahashi, Y.; Sazaki, G.; Sugimoto, K.; Nonaka, T.; Masai, E.; Fukuda, M.; Senda, T. *J. Mol. Biol.* **2002**, *321*, 621−636.

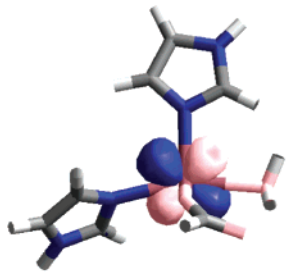

Figure 5. MO surface plots of the redox active orbital d_{yz} (highest occupied spin-down orbital) of DHBD.

Table 4. MO Compositions for the Spin-Down Valence Metal-Based Orbitals in the Electronic Ground State from the DFT Calculations of DHBD

MO #	label	energy	*yz*	*xy*	*xz*	x^2-y^2	z^2	$4p_z$	Glu
52	x^2-y^2	−4.919	0.2	0.7	0.2	46.6	11.9	1.4	1.8
51	z^2	−5.956		0.1	2.3	19.9	58.7	3.7	2.5
50	*xy*	−6.499	6.1	42.6	34.8		2.1		7.2
49	*xz*	−6.631	8.5	30.4	47.8	0.3	0.7	0.2	4.4
48	*yz*	−7.222	77.9	15.2	0.5	0.8	0.4		0.3

Table 5. Experimental and Calculated Transition Energies (cm^{-1}) for DHBD

	experimental	E.S. calculation[a]
x^2-y^2	11 000	14 260
z^2	5500	6490
xy	925	1360
xz	450	0
yz	0	0

[a] The transition energies here are from the ground-state single point calculation (G.S.) and the series of ΔSCF calculations which includes the relaxation upon excitation (E.S.).

is consistent with its having the most antibonding interaction with the ligands (i.e., it points nearly along the four bonds in the equatorial plane). The splitting of the t_{2g} orbitals with $d_{xy} > d_{xz} > d_{yz}$ reflects the stronger π-donor glutamate ligand in the *x* direction as can be seen by the larger amount of glutamate ligand character in the d_{xy} and d_{xz} orbitals (Table 4). The calculated transition energies (Table 5) are similar to experiment with the greatest deviation in the highest energy d → d transition. Thus, the calculations are reasonably consistent with the experimental spectroscopic data and can be used to obtain further insight into the electronic structure.

The electronic structure is generally consistent with an approximate square planar geometry, but the $d_{x^2-y^2}$ and d_{z^2} orbitals mix with each other. Additionally, the d_{z^2} level mixes with the d_{xz} orbital. This provides a mechanism for spin−orbit coupling between the formally $d_{x^2-y^2}$ and d_{z^2} levels, which provides an explanation for the signs in the low-temperature MCD spectrum (see Discussion). The mixing which is forbidden in C_{4v} symmetry becomes allowed due to the tilt of the axial histidine (~9° off the normal of the square pyramid) toward the water trans to the glutamate (*x*-direction) and the asymmetry of the ligands in the equatorial plane associated with the short glutamate ligand (Scheme 3). Both the short glutamate and the tilt of the axial histidine away from the glutamate lead to a C_s-effective site symmetry which allows the $d_{x^2-y^2}$, d_{z^2}, and d_{xz} orbitals to mix because they all transform as A′.

Scheme 3

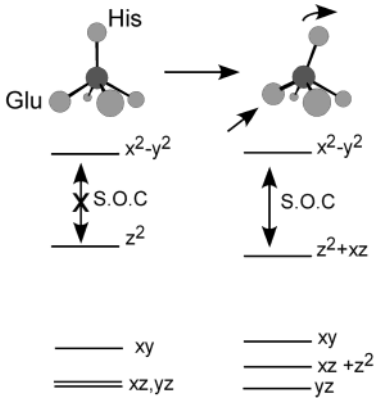

The calculated 4p character (Table 4) can be compared to the experimental 4p mixing obtained from the XAS pre-edge (vide supra). The 4p mixing comes predominantly from the $4p_z$ orbital with the majority (3.7 of 5.3%) into the d_{z^2} orbital as expected for a square pyramidal site. Additionally, there is 1.4% mixing into the $d_{x^2-y^2}$ orbital due to the C_s symmetry.

The ground state can be best described as a localized d_{yz} orbital (Figure 5, note the spin−orbit mixing among the t_{2g} orbitals is small, vide supra). This orbital is lowest because the d_{xz} and d_{xy} orbitals are antibonding with the glutamate donor ligand in the *x* direction. This orbital is well oriented to overlap and transfer an electron to dioxygen at the open position of the square pyramidal Fe(II) site.

(2) DHBD-O_2. The ferrous resting site in DHBD is five-coordinate with an open coordination position on the iron which, according to the X-ray structure,[10] is accessible to small molecules including the reversible binding of NO. The FMO analysis (above) shows that the redox active MO on the iron is well oriented for electron transfer to the π^* acceptor orbital on the O_2. However, the reaction of dioxygen with the resting ferrous site of DHBD is very slow. Kinetic studies[58] determined an apparent pseudo-first-order rate constant of $(0.7 \pm 0.1) \times 10^{-3}$ s^{-1}, corresponding to an activation barrier of $\Delta G^{\ddagger} \approx 22$ kcal/mol, for the autoxidation of the ferrous active site to a ferric species and superoxide. DFT calculations have been used to explore the origin of this low reactivity for a five-coordinate ferrous site with O_2.

To evaluate the thermodynamics of the reaction of dioxygen with DHBD, the active site of high-spin ferrous DHBD was optimized for two different models (coordinates in Supporting Information) and using two different density functionals (B3LYP and BP86). Triplet O_2 ($S = 1$) was optimized in the same manner. For both models, a very similar geometric and electronic description of the 5C DHBD complex was obtained (table in Supporting Information). The main difference in the geometry optimized active site structure of DHBD relative to the X-ray crystal structure is the formation of a strong hydrogen bond between the uncoordinated glutamate oxygen and the adjacent water ligand (Wat3001 in ref 10) leading to a trigonal bipyramidal distortion of the Fe site. In the protein, the active site is stabilized by an extensive hydrogen bonding network: There is a hydrogen bond between the distal oxygen of glutamate and Ser248, the adjacent water ligand (Wat3001)

(58) Vaillancourt, F. H.; Labbe, G.; Drouin, N. M.; Fortin, P. D.; Eltis, L. D. *J. Biol. Chem.* **2002**, *277*, 2019−2027.

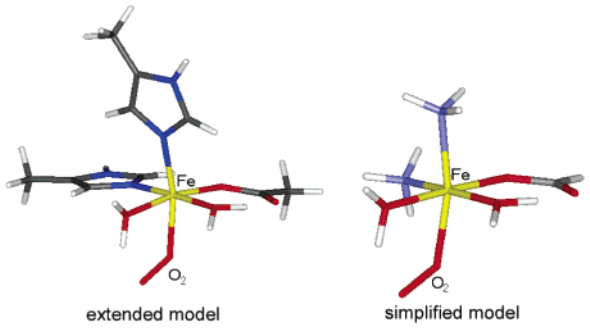

Figure 6. Structure of geometry optimized DHBD-O_2 (extended and simplified model, B3LYP).

Table 6. Thermodynamics of the Binding of O_2 to DHBD

			ΔE[a]		correction terms[a]		
method	model		LanL2DZ	TZV	+solvent[b]	+ZPCE $-T\Delta S$[c]	ΔG[a]
BP86	simple		−11.0	−16.8	−0.5	+14.3	−3.0
	extended	with H-bond	−12.3	−16.9	+1.2	+15.5	−0.2
		no H-bond	+6.0	+2.1	−3.2	+15.5[d]	+14.4
B3LYP	simple		+4.7	−4.9	−0.7	+14.2	+8.6
	extended	with H-bond	+0.9	−4.0	+1.0	+14.9	+11.9
		no H-bond	+15.9	+15.6	−0.9	+14.9[d]	+29.6

[a] All values in kcal/mol. [b] Solvent: including a solvent sphere in the calculation using the polarized continuum model (PCM) and a dielectric constant of $\epsilon = 4.0$. [c] Entropy ($T = 298$ K) and zero point correction energy (ZPCE) were calculated using the LanL2DZ basis set. [d] Using corrections of the fully optimized model (with H-bond).

forms a hydrogen bond with a noncoordinated water and Asp244, and the water ligand trans to Glu (Wat3012) is hydrogen bonded to a noncoordinated water and to His195.[10]

Dioxygen was placed in the open position of DHBD trans to Me-imidazole (equivalent to His146 in ref 10), and the complex was optimized. Optimizations with different starting geometries converged to the same structure (Figure 6).

The geometric and electronic structure of DHBD-O_2 is found to be dependent on the spin state ($S = 1, 2, 3$) and the density functional used (B3LYP vs BP86). Using B3LYP with $S = 3$, we determined that the geometry optimized structure corresponds to hs Fe(II) ($S = 2$) and triplet O_2 (ferromagnetically coupled) with a long Fe−O bond, 2.48 Å. Thus, no complex, different from the reactants, was formed. For both the B3LYP and the BP86 calculations, the $S = 2$ state is lower in energy than the $S = 1$ state, and the electronic structure corresponds to a ferric-superoxide complex in which the Fe−O bond length is dependent on the functional used.

The Gibbs free reaction energies (ΔG) for the binding of O_2 to DHBD, including the effects of the dielectric of the protein ($\epsilon = 4.0$), zero-point correction energy (ZPCE), and an entropy correction, are given in Table 6. The largest term is the entropy/ZPCE term due to the increased order in the O_2 bound complex. The calculated thermodynamic parameters of the reaction of DHBD with dioxygen vary only slightly between the simplified and extended models (~3 kcal/mol, see Table 6). This is consistent with former studies which demonstrate that NH_3 groups are reasonable substitutes for imidazoles in enzyme active site models.[59,60] However, there is a difference between the free energy values obtained using the pure DFT functional

(59) Gewirth, A. A.; Solomon, E. I. *J. Am. Chem. Soc.* **1988**, *110*, 3811−3819.
(60) Siegbahn, P. E. M. *J. Comput. Chem.* **2001**, *22*, 1634−1645.

Table 7. Geometric and Electronic Structure Parameters for DHBD-O_2

		geometric parameters[a]		spin densities		Mulliken charges	
method	model	r(Fe–O)	r(O–O)	Fe	ΣO_2	Fe	ΣO_2
BP86	simple	1.88	1.37	+3.03	+0.64	+0.60	−0.28
	extended	1.88	1.37	+2.95	+0.69	+0.49	−0.31
B3LYP	simple	2.08	1.34	+4.05	−0.58	+0.94	−0.31
	extended	2.11	1.35	+4.09	−0.64	+0.89	−0.33

[a] Bond lengths in Å.

Scheme 4

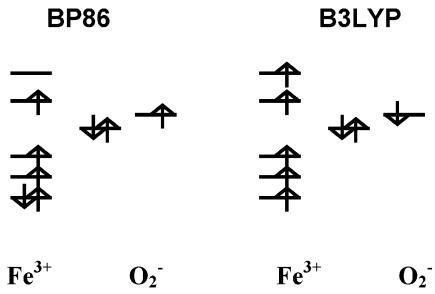

BP86 and the hybrid-functional B3LYP. With BP86, the reaction is calculated to be thermoneutral, while with B3LYP it is endergonic with $\Delta G \approx 12$ kcal/mol (Table 6).

From Table 6, it is clear that the main contribution to the observed functional dependence is from the electronic energy term. The reactants (5C DHBD and O_2) have a geometric and electronic structure independent of the functional applied (see Supporting Information). Hence, the stability of the reactants is not affected by the choice of theory. The different density functionals affect the stability of the product DHBD-O_2 complex, leading to different ΔG values for the reaction.

Comparisons of the geometric and electronic structure of DHBD-O_2 between the two models and two functionals are listed in Table 7. The simplified and extended models show very similar results in the geometric and electronic parameters. Although both functionals define DHBD-O_2 as a ferric-superoxide complex, the Fe−dioxygen bonding description differs greatly. The complex has a much shorter Fe−O bond and a slightly longer O−O bond (Table 7) when the BP86 function was used. In addition, large variations can be observed in the spin distribution: BP86 describes the complex as an intermediate spin ferric complex with $S = {}^3/_2$ ferromagnetically coupled to a superoxide $S = {}^1/_2$ ($S_{tot} = 2$), while B3LYP presents a high spin $S = {}^5/_2$ ferric complex, antiferromagnetically coupled to the superoxide with $S = {}^1/_2$ ($S_{tot} = 2$) (see Scheme 4).

The DHBD-O_2 complex described by BP86 is stabilized by a strong and covalent Fe−O bond which lowers the total energy. In contrast, application of B3LYP leads to a longer, weaker Fe−O bond. Consequently, the product is less stable, and the free reaction energy is raised by ~12 kcal/mol and is thermodynamically less favorable.

An important feature of the active site of DHBD is the presence of two water ligands. These water ligands can in principle help stabilize the ferric superoxide species by deprotonation or H-bonding; thus, their effects on lowering or raising the reaction energetics were explored. The effect of deprotonation of one of the water ligands was investigated for the extended model using the B3LYP functional. The water ligand opposite to the acetate was deprotonated, and the complex was

Table 8. MO Compositions for the Valence Metal-Based Orbitals and the Relevant Substrate Orbitals in the Electronic Ground State from the DFT Calculations of DHBD-DHB

MO #	# e⁻	label	energy	*yz*	*xy*	*xz*	x^2-y^2	z^2	$4p_z$	DHB	His	Glu
					Spin-up							
64	1	DHB	−4.240	−	2.6	4.5	0.1	6.0		64.4	1.2	17.5
65	1	x^2-y^2	−3.644			0.1	57.9		0.5	21.0	13.8	0.3
					Spin-down							
59	1	DHB	−4.542		0.8	2.8	0.2	1.6	0.6	85.8	0.2	1.9
60	1	Glu	−4.477	0.6		0.2		1.6	0.1	6.7	0.1	89.6
61	1	*xy*	−2.864	4.0	84.0		0.1	2.1	0.1	2.0	4.5	0.1
62	0	*yz*	−2.371	83.0	3.5	2.0		1.5		1.3	1.4	5.2
63	0	*xz*	−2.151	1.1		66.7	0.1	7.2	1.8	5.1	9.4	5.5
64	0	z^2	−1.953	1.2	2.5	9.2		66.1	3.1	13.0	3.0	2.7
65	0	His	−1.135	0.1	0.3	1.7	0.1	2.5		1.0	90.3	0.5
66	0	DHB	−0.742				0.8		0.2	84.2	7.8	0.5
67	0	His	−0.562			0.1	1.4		0.1	12.0	86.2	0.1
68	0	His/DHB/x^2-y^2	−0.521	0.1	0.1	0.1	14.2		0.2	4.0	74.1	0.1
69	0	His/DHB/x^2-y^2	−0.419		1.1	2.0	21.7	0.6	0.4	11.6	57.1	0.7
70	0	His/DHB/x^2-y^2	−0.339	0.1	0.1	0.7	15.9	0.2	0.1	16.8	68.9	0.1

reoptimized. The free energy of the deprotonation reaction was calculated (B3LYP/TZV, considering the solvent effect) using a theoretical value of $\Delta G_{solv}(H^+) = -262.23$ kcal/mol (T = 298 K) for the proton, which has been determined by large scale ab initio calculations on small water clusters $(H_2O)_n$.[61] The free energy of the deprotonation is exergonic with $\Delta G = -2$ kcal/mol, slightly favoring a DHBD-O_2 with one water and one hydroxide ligand rather than two water ligands, which brings the overall charge of the metal site to zero, thus maintaining site neutrality. The deprotonation of the Fe-bound water has little effect on the reaction energetics, however, changing the overall ΔG of the reaction by only 2 kcal/mol.

The effect of hydrogen bonding on the stability of the DHBD-O_2 complex was investigated using both the BP86 and the B3LYP functional. The equatorial water hydrogen-bonds to the distal oxygen of the superoxide (1.74 Å (BP86), 1.65 Å (B3LYP)), weakening the water O−H bond (lengthened by 0.4 Å for both BP86 and B3LYP) and leading to increased hydroxide character. This helps to stabilize the ferric superoxide complex in a way that could not occur in the actual protein site due to hydrogen bonding with residues in the protein pocket: this water ligand (Wat1012) hydrogen-binds to His195 and a noncoordinated water molecule according to the X-ray structure.[10] The effects of eliminating the hydrogen bond to the superoxide were explored by rotating the water ligand about the Fe−water bond. This complex without the hydrogen bond was partially reoptimized (for coordinates, see Supporting Information). The complex was destabilized by ∼15 kcal/mol (BP86) and by ∼18 kcal/mol for B3LYP, leading to a free reaction energy of $\Delta G = +14$ kcal/mol (BP86) or $\Delta G = +30$ kcal/mol (B3LYP) (see Table 6). These values are in general agreement with experiment, which determined via kinetic studies an activation barrier of $\Delta G^{\ddagger} \approx +22$ kcal/mol for the autoxidation of the ferrous active site to a ferric species and superoxide.[58]

Another structural feature that could reduce reactivity is the steric effect of the OH-group of Tyr250, which is only 3.7 Å from the iron above the open coordination position. When BP86 was used, a partially optimized structure with a fixed N_{ax}−Fe−O angle of 150° (as compared to 172° in the fully optimized structure) was carried out to evaluate this possible steric hindrance. These calculations show that the peroxo moves between the two water ligands, which limits the sterics involved and raises the energy by 10.4 kcal/mol.

Finally, it is possible that a kinetic barrier associated with the binding of O_2 to DHBD, either due to structural changes or a redistribution of spin densities or both, may contribute to the relative lack of reactivity. The energetics along this coordinate were evaluated by gradually elongating the Fe−O bond from the optimized distance (1.88 Å) using the BP86 functional. Partial optimizations were carried out at each step. At an elongation of 0.5 Å away from the optimized bond length (resulting in r(Fe−O) = 2.38 Å), the electronic structure obtained no longer corresponds to the geometry optimized structure in BP86 (intermediate spin Fe(III), $S = {}^3/_2$, ferromagnetically coupled to superoxide, $S = {}^1/_2$). Instead, in agreement with the electronic structure of the B3LYP calculation, the complex can be described as a hs Fe(III), $S = {}^5/_2$, antiferromagnetically coupled to superoxide, $S = {}^1/_2$. While a crossing of potential energy surfaces has taken place, no reaction barrier was found which could contribute to the experimentally observed low reaction rate.

In conclusion, the thermodynamics of the reaction of DHBD with O_2 somewhat depend on the functional used. BP86 gives a description of DHBD-O_2 with a strong, covalent Fe−O bond, which stabilizes the product and lowers the free energy. When B3LYP was used, the Fe−O bond is longer and weaker, and the reaction is strongly uphill. Inclusion of the hydrogen-bonding network in the enzyme active site which prevents the H_2O ligand from hydrogen bonding to the O_2 gives free reaction energies of $\Delta G = +14$ kcal/mol (BP86) and +30 kcal/mol (B3LYP), in general agreement with experiment ($\Delta G^{\ddagger} \approx 22$ kcal/mol). Steric restrictions at the site can further destabilize the product by ∼10 kcal/mol. Thus, while the choice of functional changes the energetics due to differences in covalency, the autoxidation of the 5C site is thermodynamically unfavorable regardless of the functional used.

(3) DHBD-DHB. For these calculations, a coordinate system was chosen such that the glutamate Fe−O bond is *z*, the short substrate Fe−O bond is closest to *x*, and the longer substrate Fe−O bond is closest to *y*. The ground-state orbital energies and one-electron wave functions are summarized in Table 8. The five spin-down d-orbitals (spin-unrestricted) are the highest

(61) Tawa, G. J.; Topol, I. A.; Burt, S. K.; Caldwell, R. A.; Rashin, A. A. *J. Chem. Phys.* **1998**, *109*, 4852−4863.

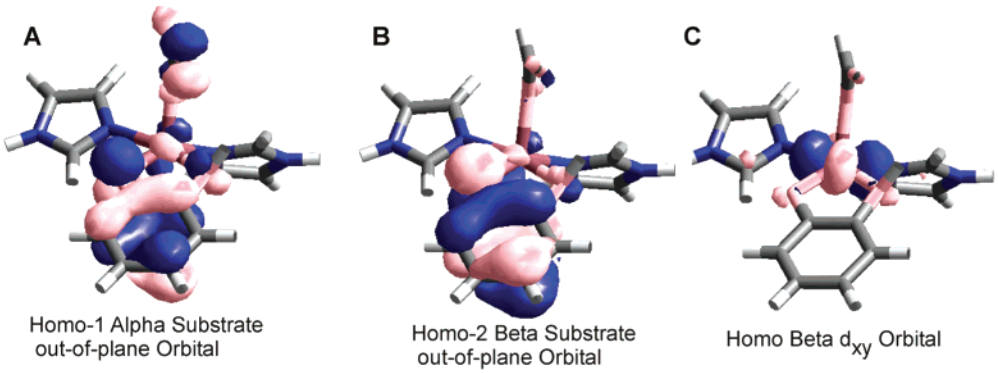

Figure 7. MO surface plots of the (A) alpha and (B) beta occupied out-of-plane substrate orbitals of DHBD-DHB and (C) the occupied redox active metal (beta d_{xy}).

occupied MO (61, d_{xy}), the lowest three unoccupied MOs (62−64), and the $d_{x^2-y^2}$ orbital that is the highest in energy and mixed with the DHB and the histidine valence orbitals (68−70). The overall ordering of the d-manifold ($d_{xy} < d_{yz} < d_{xz} < d_{z^2} < d_{x^2-y^2}$) is consistent with a distorted square pyramidal ligand field as expected from spectroscopy. However, 10 *Dq* is higher, and the t_2 and e sets are more split than observed experimentally (Figure 2, right; note that the t_2 orbital labels in the figure correspond to an arbitrary *z*-axis of the $^5T_2$ Hamiltonian), indicating overly covalent interactions in the BP86 calculation. The 4p mixing is predominantly into the d_{z^2} orbital from the $4p_z$ orbital as observed experimentally (Figure 2, right). The d-manifold is deeper in energy than in the DHBD calculation due to the loss of positive charge upon monoanionic substrate coordination and the pseudo-four-coordinate geometry of the active site associated with the long Fe−$O_{substrate}$ bond (2.53 Å). This leads to the significant mixing of the metal and ligand orbitals as compared to DHBD.

The DHB substrate has high-lying occupied orbitals that have significant mixing with the metal: 13% into the α-occupied orbital #64 and 4% into the *β*-occupied orbital #59. This mixing is important as it provides low energy ligand-to-metal charge transfer to orbitals (d_{xz} and d_{z^2}) well suited for overlap with the O_2 π^* acceptor orbitals. The α- and *β*-occupied out-of-plane substrate orbitals of DHBD-DHB and the occupied redox active metal orbital (d_{xy}) are shown in Figure 7.

Discussion

Geometric and Electronic Structure of DHBD and DHBD-DHB. From the ligand-field splitting of the ^5E_g excited state obtained from CD and MCD spectroscopy and the XAS pre-edge intensity distribution and splitting pattern, the above studies have shown that both DHBD and DHBD-DHB have five-coordinate square pyramidal ferrous active sites. Upon substrate binding, the Δ^5E_g splitting decreases from 5500 to 4500 cm^{-1} and the 4p mixing from the pre-edge redistributes, indicating a perturbation in the axial direction, where upon substrate binding there is a stronger axial interaction.[62] By comparison of the X-ray crystal structures of DHBD and DHBD-DHB, the axial direction shifts from the histidine to the glutamate ligand. Glutamate is a stronger donor than histidine which would be expected to raise the energy of the d_{z^2} orbital and lower that of the $d_{x^2-y^2}$ orbital, as observed in MCD, as well as increase the 4p mixing in the *z* direction, as observed in the XAS pre-edges. Additionally, the value of δ decreases upon substrate binding, reflecting a larger t_{2g} splitting and thus a stronger d_π Fe(II)−substrate bond.

The EXAFS bond lengths, MCD/CD, and pre-edge results can be used to evaluate various literature proposals for the geometry of DHBD, DHBD-DHB, 2,3-CTD, and a model compound.[10,18,20,63] From a comparison to the X-ray crystal structure of DHBD to the EXAFS bond lengths, the short distance at 1.98 Å is the glutamate ligand and the four remaining ligands are at 2.12 Å. Two prior EXAFS results have been reported for the extradiol dioxygenase 2,3-CTD. One indicated that the site was six-coordinate, and the other found five ligands at 2.09 Å.[20,21] The results reported here indicate, from CD/MCD and pre-edge analysis, a five-coordinate site. The appearance of a short bond for Fe(II)−glutamate in the crystal structure (1.96 Å)[10] is more consistent with the EXAFS reported here. The geometry optimized structure of DHBD has a longer Fe−glutamate bond (2.1 Å) which is due to a hydrogen bond with an adjacent coordinated water; this increases upon geometry optimization. This interaction is limited in the protein by an extensive hydrogen-bond network where the water ligands are hydrogen bonded to ordered waters, histidine, and asparatate residues in the protein pocket. Additionally, these are coordinated as water in DHBD because there is no change observed by MCD between pH = 7 and 8. The pK_a of water would have to be <6.5 (not reasonable for Fe(II)), or >9, for the protonation change to not be observed. Thus, the resting site has a charge of +1.

For DHBD-DHB, two short distances are observed at 1.98 Å that are attributed to the glutamate and the short substrate bond, with the remaining three ligands at 2.14 Å. Two prior EXAFS results have been reported for 2,3-CTD-catechol. One indicated a six-coordinate site, and the other indicated one ligand at 1.93 and four at 2.10 Å.[20,21] The latter attributed the split in the shell due to the asymmetric binding of substrate.[21] The results reported here with two ligands with short distances are more consistent with a short Fe−substrate and a short Fe−glutamate bond, which are 1.98 and 1.99 Å, respectively, in a recent five-coordinate DHBD-DHB structure.[57] From the geometry optimized calculations on DHBD-DHB, the long water in the crystal structure (2.4 Å, Scheme 1) backs out of the iron center to 2.56 Å, and therefore the five ligands observed in the CD/MCD and XAS studies are the two substrate bonds, the

(62) This decrease in the splitting of the e_g orbitals is also seen for 2,3-CTD. The MCD spectra had been reported for 2,3-CTD-catechol (ref 9) to indicate an increase in the e_g splitting relative to 2,3-CTD. However the $d_{x^2-y^2}$ orbital is at 11 200 cm^{-1} and the 13 330 cm^{-1} band is a weaker CT transition.

glutamate, and the two histidines. The asymmetric binding of the substrate from the EXAFS analysis is consistent with UV rR spectroscopy which showed that the substrate is bound as a monoanion, and with the crystal structure of a ferrous model complex which indicated monoanionic binding of substrate with bond lengths of 2.26 and 1.95 Å.[18,63]

The majority of ferrous proteins and model systems studied to date have all of their MCD d → d transitions with positive intensity.[33] This is a large deviation from the sum rule (equal magnitude and opposite sign MCD intensity for excited states) that derives from spin−orbit coupling of higher components of the low symmetry split $^5T_2$ into the ground state. In DHBD and DHBD-DHB, the higher energy transition (into the $d_{x^2-y^2}$ orbital) has small negative MCD intensity. This observation indicates that for this site structure the $d_{x^2-y^2}$ and d_{z^2} states spin−orbit couple (SOC) with each other. Because these orbitals cannot directly spin−orbit couple (there is no matrix element of the orbital angular momentum, L), this requires that one of the t_2 orbitals mixes into the e set providing a mechanism for SOC. From the MO compositions of DHBD (Table 4), it can be seen that the d_{z^2} orbital has mixing with the d_{xz} orbital (the highest levels of the t_2 set). This d_{xz} mixing allows SOC of the formally d_{z^2} orbital with the $d_{x^2-y^2}$ orbital via the L_y SOC operator. This d_{z^2}/d_{xz} mixing derives from the combined tilt of the axial histidine off the normal to the plane of the square pyramid and from the short Fe−glutamate bond leading to effective C_s symmetry as shown in Scheme 3. The negative band at 11 000 cm^{-1} in Figure 1 is significantly less intense in DHBD-DHB, consistent with this complex having a stronger axial direction and less C_s distortion. Thus, the MCD spectral pattern reflects this structural feature in the extradiol dioxygenase active site.

Dioxygen Reactivity. The spectroscopic results can be correlated to quantum chemical calculations to gain insight into the enzyme reactivity. The relative lack of dioxygen reactivity for the resting DHBD active site is intriguing: according to X-ray structures, the active site is accessible to small molecules including reversible binding to NO; the iron has an open coordination position; FMO studies show a favorable overlap between the redox active MO on the ferrous center and an incoming dioxygen; and there is no kinetic barrier, steric [as analyzed above, the steric effect of the OH-group of Tyr250 raises the reaction energy by only ∼10 kcal/mol] or electronic, for O_2 binding. Thus, the low experimentally observed reaction rate must be due to thermodynamic effects.

The calculated electronic structure of DHBD-O_2 corresponds to a ferric-superoxide complex with a total spin $S = 2$. The Fe-dioxygen bonding description depends on the density functional used, though: The BP86 functional gives a intermediate spin Fe^{III} ferromagnetically coupled to the superoxide forming a strong covalent Fe−O bond, while B3LYP describes the complex as a high-spin Fe^{III} antiferromagnetically coupled to the superoxide by a weaker, longer bond.

The thermodynamics of the reaction of dioxygen with the resting 5C ferrous site can be conceptually divided into three steps: a redox term for the one-electron transfer to Fe(III) and superoxide, an entropy term ($-T\Delta S$), and a term associated with the formation of the Fe−O bond (see Scheme 5).

The one-electron transfer from the ferrous site to dioxygen is unfavorable for both species. The reduction of dioxygen to

Scheme 5

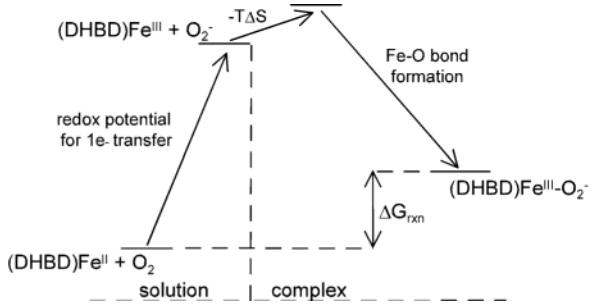

superoxide decreases the O−O bond order by $^1/_2$, and the electron pairing in one of the π^* orbitals leads to a loss of exchange stabilization. The experimental value for the reduction potential for the O_2/O_2^- couple in an aqueous solution is −0.33 V (1 atm vs NHE).[64] This value should be even lower in the protein site environment with a low dielectric constant [calculations estimate a redox potential $E° < -1$ V]. Additionally, the oxidation of the ferrous active site to a ferric species can be expected to have a high potential in the low dielectric of the protein with this set of poor donor ligands. The Fe(II)/Fe(III) midpoint potential, determined by EPR spectroscopy, for the closely related site in phenylalanine hydroxylase (PAH) is $E° = +0.19$ V.[65] This, however, is a lower limit as water likely coordinates to Fe(III) stabilizing the oxidized site and lowering the potential. In lipoxygenase, an enzyme with a similar innocent ligand set, which is 5C on oxidation, the Fe(II)/Fe(III) potential was estimated to be >600 mV.[66] Together, these lead to a great energy barrier, and the redox step to form Fe(III) and superoxide is energetically unfavorable.

The entropy term for DHBD-O_2 complex formation further increases the thermodynamic barrier by ∼15 kcal/mol. In contrast, the Fe−O bond formation is energetically favorable. A comparison of the electronic structures and free reaction energies obtained with the two density functionals used shows that a stronger Fe−O bond (BP86) lowers the overall reaction energy. However, in the absence of hydrogen bonding between the coordinated water and the superoxide, this stabilization is not enough to drive the overall reaction. Additional factors, in particular, deprotonation of a water ligand, were considered; however, none changed the overall energetics of this reaction to a significant amount. In conclusion, the Fe−O bond formation does not provide enough stabilization energy to overcome the high redox potential of the one-electron reduction of O_2 and the unfavorable entropy term.

In contrast to the reaction of DHBD with O_2, the reaction of DHBD-DHB with O_2 is very fast ($k_{cat} = 1350\ s^{-1}$) and leads to ring cleavage.[29] There are several possible contributions to this large increase in reactivity: (1) substrate binding may lower the redox potential by enhancing the stability of the ferric ion (vide supra), (2) the trans effect of the stronger axial ligand (glutamate relative to the histidine) could increase the interaction with acceptors such as O_2 or more favorably orient the redox active orbital, (3) the protein environment trans to the glutamate ligand is better able to stabilize and Fe(III)-bound O_2^-, and (4)

(63) Chiou, Y.-M.; Que, L., Jr. *Inorg. Chem.* **1995**, *34*, 3577−3578.
(64) Sawyer, D. T. *Oxygen Chemistry*; Oxford University Press: New York, 1991.
(65) Hagedoorn, P. L.; Schmidt, P. P.; Andersson, K. K.; Hagen, W. R.; Flatmark, T.; Martinez, A. *J. Biol. Chem.* **2001**, *276*, 22850−22856.
(66) Nelson, M. J. *Biochemistry* **1988**, *27*, 4273−4278.

the substrate can allow two-electron reduction of O_2 which is more favorable than the one-electron chemistry.[67]

In the presence of redox inactive substrate analogues, the ferrous centers of DHBD and 2,3-CTD undergo oxidation to Fe(III), indicating that these strong donor ligands lower the potential making one-electron oxidation by O_2 more favorable. This can also be seen from the increased reactivity of the substrate bound site with NO, a one-electron process. Alternatively, calculations show that the redox active orbital in DHBD-DHB is d_{xy} (Figure 7C), which is not well aligned for transferring an electron to O_2, so the trans effect does not appear to be a significant factor. With respect to the protein environment stabilizing the Fe(III)-O_2 complex, NO binding provides a relevant probe. The stability of the NO plus substrate complex of the related extradiol dioxygenase 2,3-CTD ($K_D \approx 3.4\ \mu M$) is much higher than that of the NO complex in the absence of substrate ($K_D \approx 190\ \mu M$);[25] yet the X-ray structure of DHBD + substrate + NO (PDB ID: 1KW8)[57] indicates no significant hydrogen bonding to the bound NO^-. Importantly, the substrate has high-lying occupied orbitals (these are predominantly the alpha and beta out-of-plane oxygen symmetric and antisymmetric orbitals, $2a_1$ and $3b_1$) which could donate one or more electrons to O_2 because they have good overlap with the metal (Figure 7A and B) with 13% metal mixing in the alpha occupied substrate orbital and 4% metal mixing into the occupied beta substrate out-of-plane orbital. Calculations for DHBD-DHB indicate that these orbitals are close in energy to the d-manifold and could help stabilize the formation of a ferric-peroxide semiquinone complex as has been favored in the literature.[3,4,6] The highest occupied orbital in DHBD-DHB is the beta d_{xy} orbital on the metal (Figure 7C, −2.86 eV). The second electron would likely come from the occupied alpha substrate orbital because it is the highest energy substrate orbital and removal of this electron would allow antiferromagnetic coupling of the semiquinone to the iron, leading to stabilization of this peroxy species.

Many members of the class of mononuclear non-heme iron enzymes show increased reactivity with dioxygen upon substrate (e.g., ring-hydroxylating Rieske dioxygenases)[68] or substrate and cofactor (e.g., phenylalanine hydroxylase)[69] binding. This has been attributed to the fact that the sites in these enzymes are six-coordinate in the resting and cofactor bound forms of the enzyme and only additional binding of substrate leads to an open coordination position that allows O_2 to react with the iron.[5,67,69] As in resting DHBD, the active site of phenylalanine hydroxylase with phenylalanine and pterin bound is five-coordinate with two histidine and a glutamate ligand.[69−71] There are several possible contributions to this difference in coordination number in the resting Fe(II) site (five vs six where a water is absent in extradiol dioxygenases): (1) the lack of an internal H-bond from the monodentate carboxylate (present in both phenylalanine hydroxylase and α-ketogluterate dependent enzymes); (2) steric hindrance of the OH-group of Tyr250 in vicinity of the open coordination site in the resting DHBD structure (the protein pocket is more open in phenylalanine hydroxylase and α-ketogluterate dependent enzymes). In DHBD, the five-coordinate Fe(II) site reacts very slowly with O_2 due to the thermodynamic barrier of the one-electron reduction of O_2. However, in phenylalanine hydroxylase, the redox active pterin provides two additional electrons for the O_2 reaction. Enzymes such as the ring-hydroxylating Rieske dioxygenases, the α-ketogluterate-dependent enzymes, and pterin-bound phenylalanine hydroxylase likely remain six-coordinate until the substrate binds to prevent the two (or greater)-electron reduction of O_2 (second electron from FeS cluster, α-ketogluterate, or pterin), leading to formation of ferric-peroxide (or ferryl) species in the absence of substrate and autoxidation of the site. In DHBD, the extra electron source is the substrate. Thus, the five-coordinate site of the resting enzyme is relatively unreactive with O_2, this being a one-electron process, until the substrate binds, which allows two-electron transfer, and the reaction with dioxygen is very fast (Scheme 6).

Scheme 6

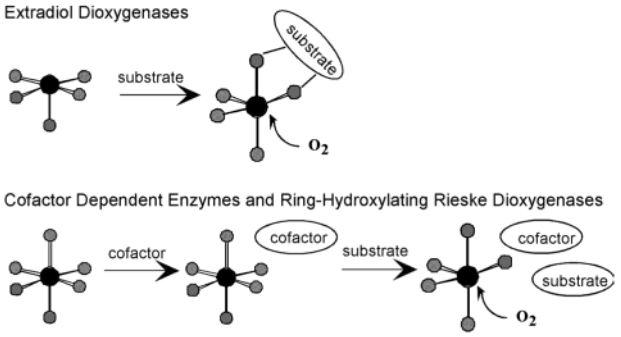

Acknowledgment. This research was supported by NIH Grant GM40392 (E.I.S.), NIH RR1209 (K.O.H.), NIH GM52381 (J.T.B.), and NSERC Grant 171359-99 (L.D.E.). M.I.D. thanks the Evelyn Laing McBain Fund for a predoctoral fellowship. F.H.V. was the recipient of an NSERC postgraduate scholarship. We would like to thank Dr. Robert Szilagyi for helpful discussions on the Gaussian 98 calculations. SSRL is funded by the Department of Energy, Office of Basic Energy Sciences. The SSRL Structural Molecular Biology program is funded by the National Institutes of Health, National Center for Research Resources, Biomedical Technology Program and by the Department of Energy, Office of Biological and Environmental Research.

Supporting Information Available: Cartesian coordinates used in the calculations and the geometry optimized structures of DHBD and DHBD-O_2 (PDF). This material is available free of charge via the Internet at http://pubs.acs.org.

JA029746I

(67) Sawyer, D. T. In *Oxygen Complexes and Oxygen Activation by Transition Metals*; Martell, A. E., Sawyer, D. T., Eds.; Plenum: New York, 1988; pp 131−148.
(68) Pavel, E. G.; Martins, L. J.; Ellis, W. R., Jr; Solomon, E. I. *Chem. Biol.* **1994**, *1*, 173−183.
(69) Kemsley, J. N.; Mitic, N.; Zaleski, K. L.; Caradonna, J. P.; Solomon, E. I. *J. Am. Chem. Soc.* **1999**, *121*, 1528−1536.
(70) Erlandsen, H.; Fusetti, F.; Martinez, A.; Hough, E.; Flatmark, T.; Stevens, R. C. *Nat. Struct. Biol.* **1997**, *4*, 995−1000.
(71) Goodwill, K. E.; Sabatier, C.; Stevens, R. C. *Biochemistry* **1998**, *37*, 13437−13445.